Evidence for a tricritical point coinciding with the triple point in $(Pb_{0.94}Sr_{0.06})(Zr_xTi_{1-x})O_3$: A combined synchrotron x-ray diffraction, dielectric, and Landau theory study

Ravindra Singh Solanki,[1] S. K. Mishra,[2] Yoshihiro Kuroiwa,[3] Chikako Moriyoshi,[3] and Dhananjai Pandey[1]

[1]*School of Materials Science and Technology, Indian Institute of Technology (Banaras Hindu University), Varanasi-221005, India*

[2]*Research and Technology Development Centre, Sharda University, Greater Noida-201306, India*

[3]*Department of Physical Science, Graduate School of Science, Hiroshima University, Japan*

(Received 23 February 2013; revised manuscript received 31 August 2013; published 27 November 2013)

We present here results of high-resolution synchrotron x-ray diffraction (SXRD) and dielectric studies in conjunction with Landau theory considerations on $(Pb_{0.94}Sr_{0.06})(Zr_xTi_{1-x})O_3$ compositions in the vicinity of the morphotropic phase boundary (MPB) to find evidence for the flattening of the free-energy surface at the MPB proposed in recent *ab initio* studies on strongly piezoelectric ceramics. SXRD results reveal that the tetragonal and pseudorhombohedral monoclinic compositions with $x = 0.515$ and 0.550 transform directly into the cubic paraelectric phase, whereas for $0.520 \leqslant x \leqslant 0.545$, the pseudotetragonal and pseudorhombohedral monoclinic compositions transform first to the tetragonal phase and then to the cubic phase. Our results reveal the existence of a triple point at $x \simeq 0.550$. It is shown that the tetragonal-to-cubic transition, irrespective of the composition, up to $x \simeq 0.545$ is accompanied with a discontinuous change in the unit cell volume and thermal hysteresis, confirming the first-order nature of this transition. However, the pseudorhombohedral monoclinic composition for $x = 0.550$ transforms directly into the cubic phase in a second-order manner. Our experimental results thus reveal a crossover from a first-order to a second-order phase transition through a tricritical point around $x = 0.550$. Landau theory calculations also confirm gradual flattening of the free-energy surface on approaching the tricritical composition $x = 0.550$. We conclude that the triple point in the $Pb(Zr_xTi_{1-x})O_3$ phase diagram is a tricritical point.

DOI: 10.1103/PhysRevB.88.184109 PACS number(s): 77.84.Cg, 61.05.cp, 68.35.Rh, 77.80.B−

I. INTRODUCTION

Lead zirconate titanate or $Pb(Zr_xTi_{1-x})O_3$ (PZT), is the most widely used piezoelectric ceramic material in electromechanical sensor and actuator devices.[1] Its x-T phase diagram contains a morphotropic phase boundary (MPB) at $x \simeq 0.520$ that separates the stability fields of pseudorhombohedral monoclinic and tetragonal phases, stable for $x \geqslant 0.530$ and for $x < 0.520$, respectively, through a thin stability region of a bridging pseudotetragonal monoclinic phase.[2,3] The physical properties, like the dielectric constant, piezoelectric constants, and electromechanical coupling coefficients, show maximum response corresponding to the MPB composition. The ground state of PZT in the MPB region and the pseudorhombohedral monoclinic Zr-rich region has been a subject of controversy,[4,5] but recent investigations suggest that the space group of the ground state of PZT near the MPB (Ref. 6) and on the Zr^{4+}-rich side of MPB is Cc.[7] Like the true ground state of PZT, the origin of a high piezoelectric response for the MPB composition has been under intense debate[8–12] in recent years.

In a pioneering paper, Fu and Cohen,[8] using first-principles calculations, have shown that the giant piezoelectric response of MPB ceramics is a consequence of flattening of the energy surface near the MPB, which can facilitate the rotation of the polarization direction from [001] pseudocubic ($[001]_{pc}$) of the tetragonal phase toward $[111]_{pc}$ of the rhombohedral phase on a symmetry plane of the intermediate bridging phase or phases in the monoclinic symmetry. Such monoclinic phases have since been discovered and are known to possess Cm (M_A),[13] Cm (M_B),[14] Pm (M_C),[15] and Cc (Refs. 2, 6, 7, and 16) space groups in different Pb-based MPB systems. Recently,[17] in a lead-free $Ba(Zr_{0.2}Ti_{0.8})O_3$-$x(Ba_{0.7}Ca_{0.3})TiO_3$ system, it has been argued that the physical properties show maximum response in the MPB region due to the existence of a tricritical point at the triple point where two first-order phase boundaries (i.e., MPB and ferroelectric-paraelectric) intersect. The presence of a tricritical point leads to a nearly vanishing polarization anisotropy (flatter free-energy surface) and can thus facilitate polarization rotation between tetragonal and rhombohedral states. The free-energy flattening arising at high temperatures due to the presence of a tricritical point at the triple point can also result in flatter free-energy surface at room temperature, leading to high piezoelectric response by means of polarization rotation for the MPB composition.[11]

Notwithstanding the significance of a tricritical point coinciding with the triple point of MPB ceramics in ensuring flattening of the free-energy surface, there is considerable controversy regarding the evidence and location of a tricritical point or points in PZT. Based on dielectric and laboratory x-ray diffraction (XRD) data, Mishra *et al.*,[18] argued in 1997 that the triple point in the PZT phase diagram is a tricritical point. The possibility of the triple point in PZT being a tricritical point has been subsequently supported by Damjanovic[11] and Kim *et al.*[19] However, based on XRD studies, Eremkin *et al.*[20] have proposed the existence of two tricritical points at $x = 0.78$ and 0.45. Based on a theoretical analysis of the dielectric data and Landau theory considerations, Noheda *et al.*[21] and Haun *et al.*[22] have also proposed two tricritical points in PZT but at $x = 0.74$ and 0.49 and $x = 0.898$ and 0.283, respectively. Whatmore *et al.*,[23] using a dielectric constant, remanant polarization, and spontaneous strain measurements, found evidence for a tricritical point at the ferroelectric-to-paraelectric transition for $x = 0.94$. A tricritical point on the cubic-to-tetragonal line of phase transition has been reported by Rossetti and Navrotsky[24] at $x = 0.38$ by calorimetric measurements. More recently, Rossetti *et al.*[25] and Porta and Lookman,[12] using Landau theory considerations, have proposed two tricritical points for PZT, one on the tetragonal

side and another on the pseudorhombohedral side at $x = 0.30$ and 0.80, respectively, across the triple point composition. The presence of two tricritical points implies that the nature of the paraelectric-to-ferroelectric phase transition is of the second order for all compositions between the two tricritical points including the MPB. Since a second-order phase transition can give rise to larger response functions than those of a first-order phase transition due to a bigger flattening of the free-energy surface, it has been argued that this may hold a clue as to the high piezoelectric response of PZT in the MPB region. However, it is not *a priori* clear from this model as to why the piezoelectric response should peak only at the MPB composition and not for the entire composition range between the two tricritical points.

The present paper was undertaken to settle the existing controversies about the existence of a tricritical point near the MPB by analyzing the nature of high-temperature cubic-to-tetragonal and cubic-to-monoclinic phase transitions using temperature-dependent dielectric and synchrotron powder XRD studies across the MPB compositions of PZT with 6% Sr doping. We also use Landau theory considerations to study the flattening of the free-energy surface on approaching the MPB from the tetragonal side. Our results present unambiguous evidence for the existence of a tricritical point at $x \simeq 0.550$ that coincides with the triple point. We have chosen 6% Sr^{2+}-doped PZT samples because they show enhanced piezoelectric properties, and the ground state of such compositions in the MPB region was recently settled unambiguously.[5,6]

II. EXPERIMENTS

Highly homogeneous samples of $(Pb_{0.94}Sr_{0.06})(Zr_xTi_{1-x})O_3$ (PSZT) with $x = 0.515$, 0.520, 0.525, 0.530, 0.535, 0.545, and 0.550 were prepared by a semiwet route, which is known to give the narrowest composition width ($\Delta x \approx 0.01$) of the MPB region in PZT (Ref. 26) and PSZT.[6] The details of PSZT sample preparation are given in our previous paper.[6] High-resolution synchrotron x-ray diffraction (SXRD) measurements as a function of temperature were carried out in the 100 to 800 K range at the BL02B2 beamline of SPring-8, Japan, at a wavelength of 0.412 Å (30 keV).[27] The dielectric measurements were performed using a Schlumberger SI-1260 impedance gain phase analyzer. For SXRD measurements as a function of temperature in the range 100–800 K, the temperature was controlled to within ± 1 K. All the SXRD measurements were carried out in the heating cycle. The dielectric measurements were carried out during both heating and cooling cycles to study the thermal hysteresis. In these measurements, the sample was heated at the rate of 1 K/min but cooled at a much slower rate (0.25 K/min) to capture genuine thermal hysteresis. The data were analyzed by Rietveld technique using the FullProf[28] software package.

III. RESULTS AND DISCUSSION

A. Dielectric studies

Figure 1 depicts the variation of dielectric constant as a function of temperature for various PSZT compositions. The peak in the dielectric constant at the Curie point of the sample occurs at a higher ($T_c{}^H$) value during the heating cycle than it does during cooling ($T_c{}^C$) of the sample. Such a thermal hysteresis in the heating and cooling cycles of the dielectric

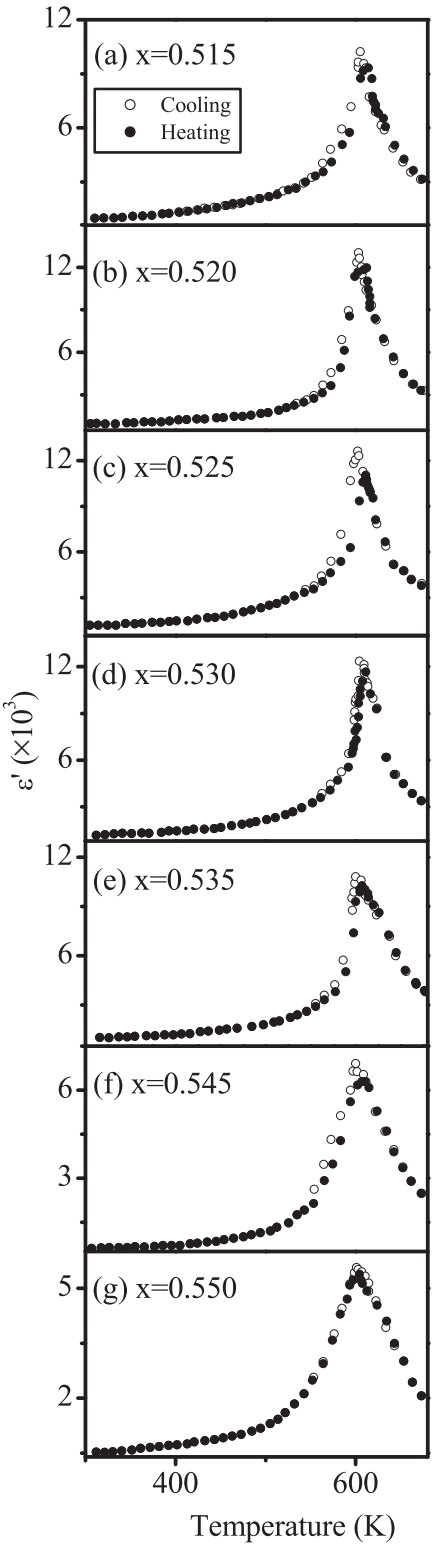

FIG. 1. Temperature dependence of dielectric permittivity (ε') of PSZT at 100 kHz for the compositions with (a) $x = 0.515$, (b) $x = 0.520$, (c) $x = 0.525$, (d) $x = 0.530$, (e) $x = 0.535$, (f) $x = 0.545$, and (g) $x = 0.550$ during heating (filled circles) and cooling (open circles) cycles.

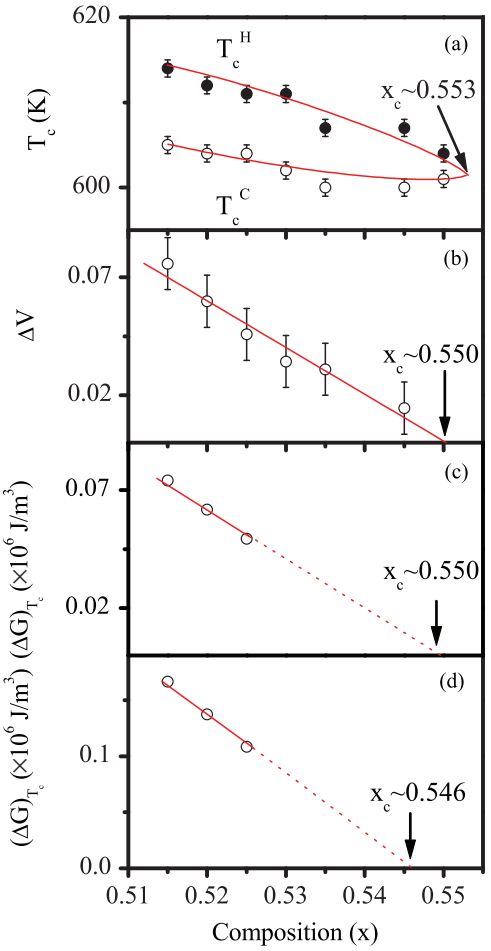

FIG. 2. (Color online) (a) The cubic-to-tetragonal phase transition temperature (T_c) during heating and cooling cycles. (b) Discontinuous change (ΔV) in the unit cell volume at the transition temperature T_c during heating. (c) Landau free-energy barrier at T_c between the cubic and the tetragonal phases of PSZT for $x = 0.515$, 0.520, and 0.525 as calculated using Landau-Devonshire theory for which we used electrostrictive coupling coefficient (Q_{11}) of PZT. (d) Landau free-energy barrier at T_c between the cubic and the tetragonal phases of PSZT for $x = 0.515$, 0.520, and 0.525 as calculated using Landau-Devonshire theory for which the value of electrostrictive coupling coefficient Q_{11} was obtained from the structural parameters of PSZT515.

measurements is known to be due to the metastability of paraelectric and ferroelectric phases below and above T_c in the cooling and heating cycles, respectively, due to a first-order phase transition.[29] Figure 2(a) shows the variation of T_c during heating and cooling cycles with composition. The thermal hysteresis $\Delta T = T_c{}^H - T_c{}^C$ is ~9 K for $x = 0.515$ and decreases with increasing x. The extrapolation of the fitted curves, for both the heating and the cooling cycles, in Fig. 2(a) yields $\Delta T = 0$ for the composition $x \simeq 0.553$. This shows that the nature of phase transition changes from first order with hysteresis to second order without hysteresis at $x \simeq 0.553$, suggesting the possibility of a tricritical point at $x \simeq 0.553$. Structural studies to be described in the next section were carried out to determine whether the tricritical point at $x \simeq 0.553$ coincides with the triple point of the PSZT phase diagram.

B. Structural studies

Pure single-phase tetragonal and pseudorhombohedral monoclinic structures of PSZT are stable for $x \leqslant 0.515$ and $x \geqslant 0.545$, respectively,[6] in our chemically homogeneous samples. In the composition range $0.515 < x \leqslant 0.525$, a pseudotetragonal monoclinic phase coexists with the tetragonal phase, while the pseudorhombohedral monoclinic phase coexists with the pseudotetragonal monoclinic phase for $0.525 < x < 0.535$.[6] The structure of the majority phase of PSZT stable across the MPB at room temperature is tetragonal ($P4mm$) for $x < 0.525$ and pseudorhombohedral monoclinic (Cm) for $x \geqslant 0.545$, with the intermediate pseudotetragonal monoclinic (Cm) phase for $x = 0.530$ (MPB composition) and 0.535, which can act as a bridging phase[2,30] between the tetragonal and the pseudorhombohedral phases. With this background information about the room-temperature structures, we now proceed to analyzing the high-temperature behavior of the various PSZT compositions.

Figure 3 depicts the evolution of the $(111)_{pc}$, $(200)_{pc}$, and $(220)_{pc}$ peaks of PSZT with $x = 0.515$ (abbreviated as PSZT515) in the temperature range 100–800 K. It is evident from this figure that at and above 625 K, all profiles are singlet. Below 625 K, the (200) and (220) cubic peaks split into two peaks, while (111) remains a singlet. These are the characteristics of a tetragonal phase. We therefore conclude that the cubic phase for $x = 0.515$ transforms directly into the tetragonal phase below 625 K.

For the PSZT compositions with $x = 0.520$ and 0.525 (abbreviated as PSZT520 and PSZT525, respectively), at room temperature a pseudotetragonal monoclinic phase coexists with the tetragonal phase. This is evidenced by the asymmetric broadening of the $(111)_{pc}$ and the triplet character of the $(220)_{pc}$ peaks. These are singlet and doublet, respectively, for the pure tetragonal phase, as can be seen from Figs. 4 and 5, which depict the evolution of SXRD profiles from 100 to 800 K. It is evident from Fig. 4 that the triplet nature of the $(220)_{pc}$ peak changes to doublet ~250 K. However, there is additional broadening in the $(111)_{pc}$ peak profile, which persists up to 525 K, as shown in Fig. 6(a). This broadening indicates the coexistence of the monoclinic phase for which $(111)_{pc}$ peak is not a singlet—unlike for the tetragonal phase, for which it is a singlet. The disappearance of this broadening ~550 K suggests that the pseudotetragonal monoclinic phase has disappeared above 525 K, leaving behind the pure tetragonal phase only as evidenced by the additional broadening of the $(200)_{pc}$ peak. To reliably determine the tetragonal-to-cubic phase transition temperature, we plot in Fig. 6(b) the full width at half maximum (FWHM) of the $(200)_{pc}$ peak as function of temperature. The FWHM of the $(200)_{pc}$ peak remains constant for $T \geqslant 625$ K, which indicates that the tetragonal phase has transformed to the cubic phase at $T \simeq 625$ K. This suggests that the pure tetragonal phase is stable in 550 K $\leqslant T \leqslant$ 625 K. In Fig. 6(b), we have only two data points in the tetragonal region, because for the third point corresponding to $T = 550$ K, $(200)_{pc}$ is clearly split into two peaks. Therefore, this data point is not included in Fig. 6(b). For PSZT525, the triplet nature of the $(220)_{pc}$ peak also changes to doublet ~325 K (Fig. 5). However, the variation of the FWHM of the $(200)_{pc}$ and $(111)_{pc}$ peak profiles with temperature (Fig. 7)

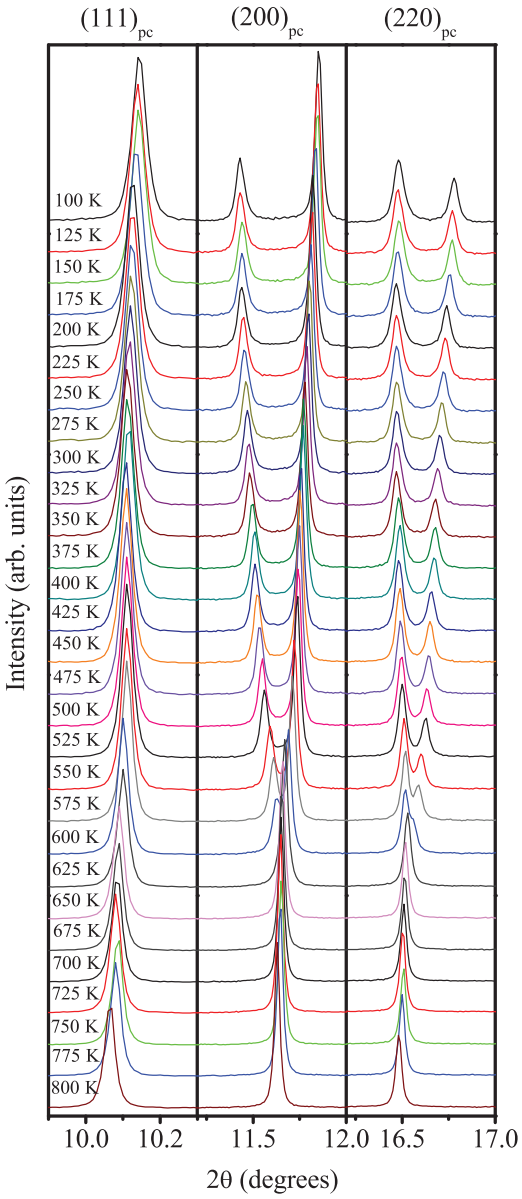

FIG. 3. (Color online) The evolution of synchrotron powder XRD profiles of the $(111)_{pc}$, $(200)_{pc}$, and $(220)_{pc}$ reflections of tetragonal PSZT515 with temperature.

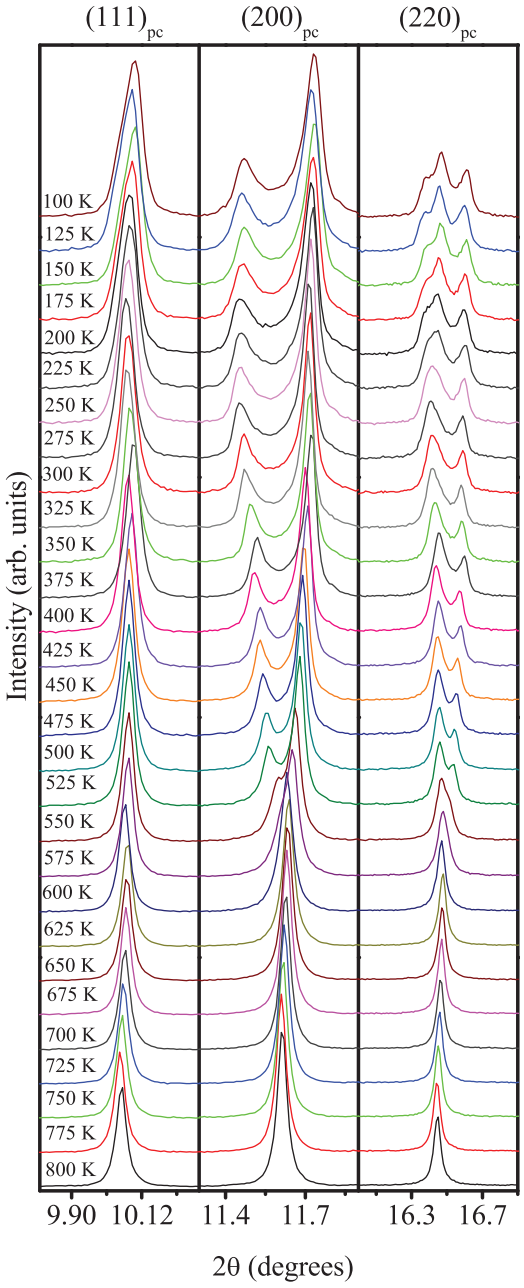

FIG. 4. (Color online) The evolution of synchrotron powder XRD profiles of the $(111)_{pc}$, $(200)_{pc}$, and $(220)_{pc}$ reflections of PSZT520 with temperature.

reveals that the structure becomes pure tetragonal at $T \gtrsim 550$ K and pure cubic above $T \gtrsim 625$ K. Thus, the sequence of phase transitions above room temperature for PSZT520 and PSZT525 is pseudotetragonal monoclinic (Cm) + tetragonal ($P4mm$) to pure tetragonal and then tetragonal to cubic ($Pm\bar{3}m$).

Rietveld refinements were carried out to confirm the conclusions arrived at from the analysis of the FWHM of the $(111)_{pc}$ and $(200)_{pc}$ peaks. We briefly discuss the Rietveld refinement results for PSZT520; similar refinements were carried out for PSZT525. Figure 8 depicts the Rietveld fits for selected perovskite reflections of PSZT520 at four representative temperatures for various plausible structural models. Coexistence of the tetragonal and monoclinic phases ($P4mm + Cm$) gives better Rietveld fit with the lower χ^2 value as compared to that for the pure monoclinic phase at 100 K. The pure tetragonal phase model is ruled out at 100 K, because the $(111)_{pc}$ peak is obviously not a singlet. This situation persists up to 225 K. In the temperature range 225 K $< T <$ 500 K, the triplet nature of the $(220)_{pc}$ peak disappears but the best fit is observed for the two-phase model only, as can be seen from the χ^2 values for the Cm, $P4mm$, and $Cm + P4mm$ structural models given in Figs. 8(c)–8(e), respectively, for a representative temperature of 450 K. This is in agreement with the FWHM analysis presented in Fig. 6. To confirm the structure or structures for temperatures between 250 and 525 K, over which the tripletlike feature of $(220)_{pc}$ disappears but additional broadening persists (Fig. 6), we first considered single-phase Cm and single-phase $P4mm$ space groups for a representative

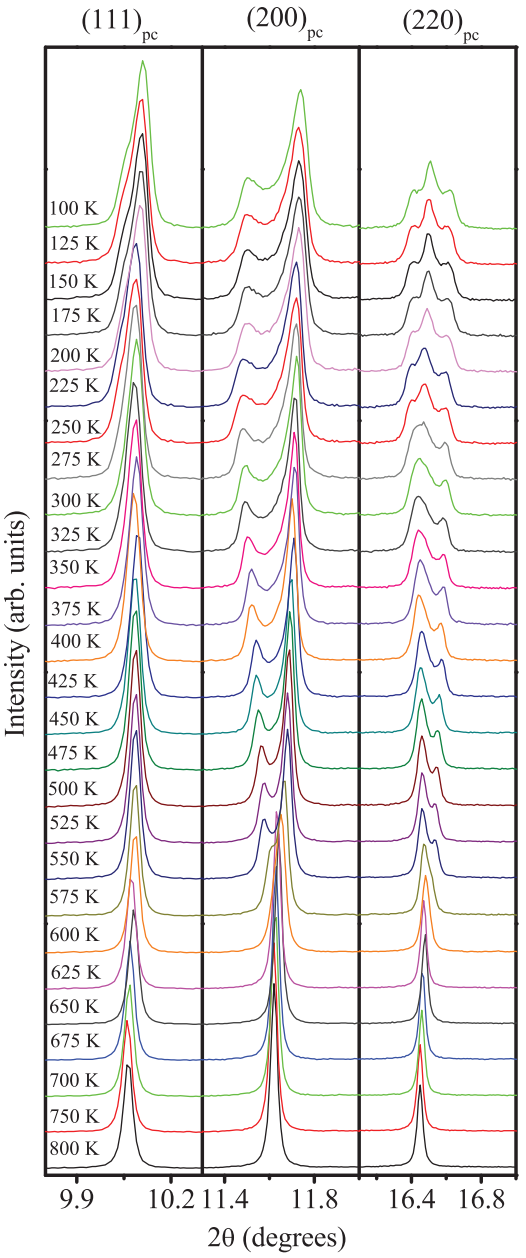

FIG. 5. (Color online) The evolution of synchrotron powder XRD profiles of the $(111)_{pc}$, $(200)_{pc}$, and $(220)_{pc}$ reflections of PSZT525 with temperature.

temperature of 450 K. The fits are shown in Figs. 8(c) and 8(d). Both single-phase models are unable to account for the $(002)_{pc}$ tetragonal peak position. We therefore considered the phase coexistence model ($P4mm + Cm$) for this temperature. This improves the quality of the fits and reduces the χ^2 value significantly. The two-phase model was found necessary up to 525 K, after which the pseudotetragonal monoclinic phase disappears, leaving behind the pure tetragonal phase as confirmed by the Rietveld refinements. Figures 8(f) and 8(g) shows the Rietveld fits using the $P4mm$ and $Pm\bar{3}m$ space groups at 550 and 800 K, respectively.

Figures 9 and 10 depict the temperature evolution of the $(111)_{pc}$, $(200)_{pc}$, and $(220)_{pc}$ peaks of PSZT for $x = 0.530$ (PSZT530) and $x = 0.535$ (PSZT535), respectively. As shown

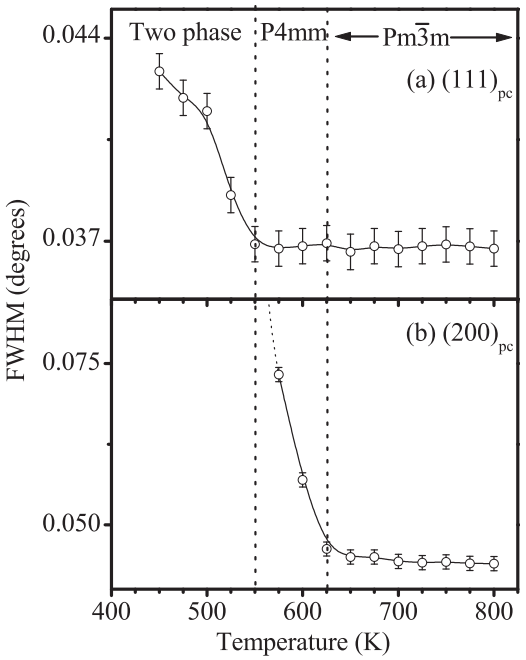

FIG. 6. The variation of FWHM of the (a) $(111)_{pc}$ and (b) $(200)_{pc}$ reflections of PSZT520 with temperature.

elsewhere[6] for PSZT530, refinements using SXRD data have shown that the pseudotetragonal monoclinic phase coexists with a pseudorhombohedral monoclinic phase,[6] both in the Cm space group, at room temperature and below to ∼260 K. At $T \lesssim 260$ K, there is a Cm-to-Cc antiferrodistortive (AFD) phase transition, the signature of which is seen in the neutron diffraction patterns only through the appearance of new superlattice peaks,[6,7] not in the SXRD patterns. The SXRD patterns of PSZT530 below 260 K are therefore not different

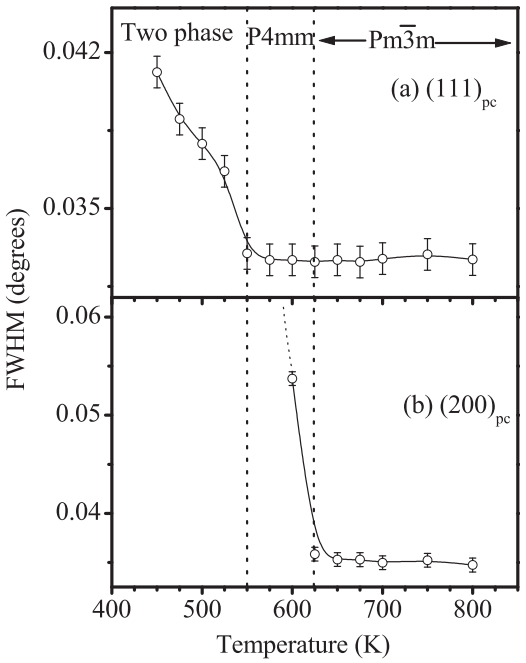

FIG. 7. The variation of FWHM of the (a) $(111)_{pc}$ and (b) $(200)_{pc}$ reflections of PSZT525 with temperature.

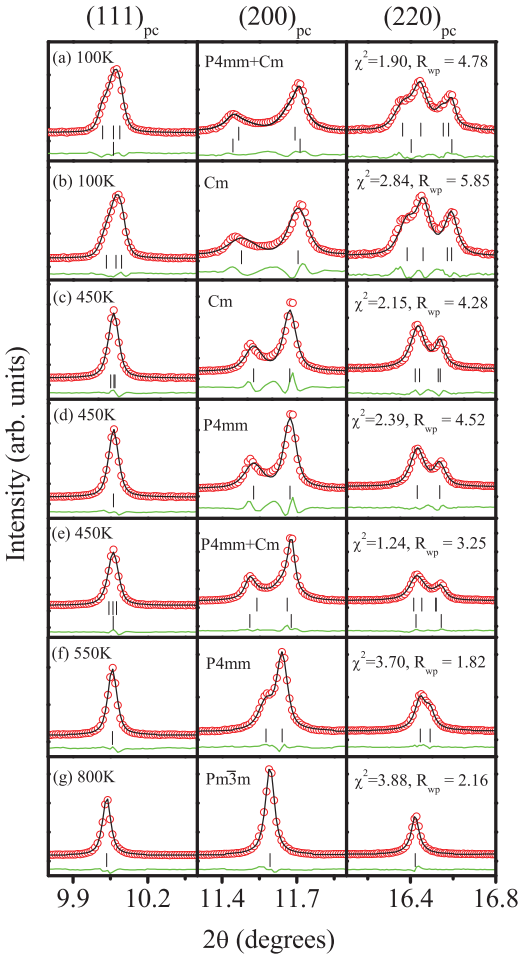

FIG. 8. (Color online) Observed (dots), calculated (central continuous line), and difference (bottom line) profiles of selected $(111)_{pc}$, $(200)_{pc}$, and $(220)_{pc}$ reflections for PSZT520 at various temperatures obtained after Rietveld refinement using plausible structural models. The vertical tick marks above the difference profiles give the positions of the Bragg reflections.

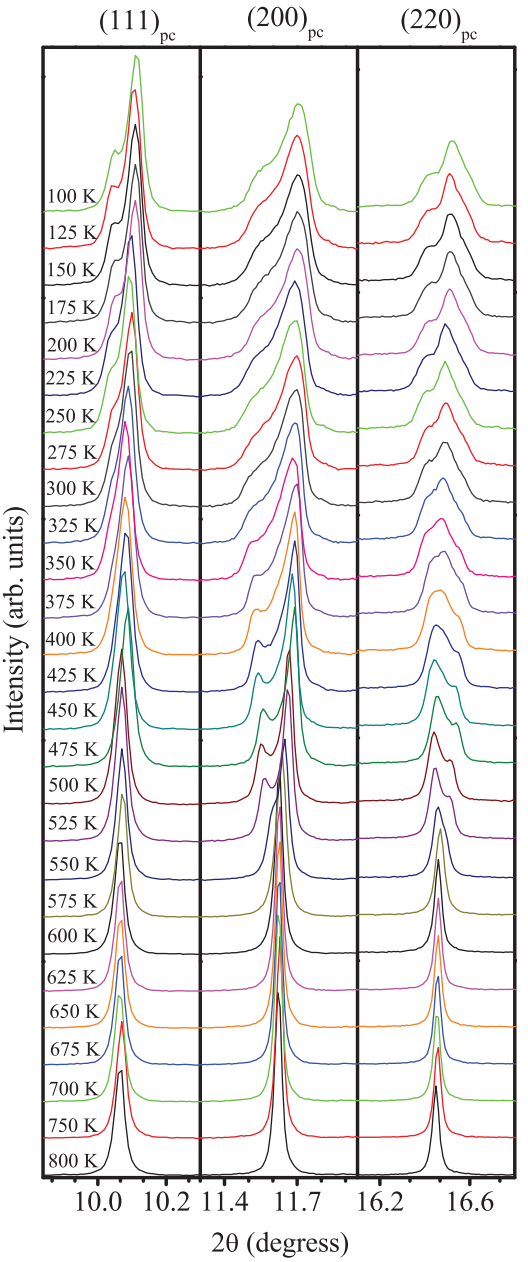

FIG. 9. (Color online) The evolution of synchrotron powder XRD profiles of the $(111)_{pc}$, $(200)_{pc}$, and $(220)_{pc}$ reflections of PSZT530 with temperature.

from those above this temperature up to ∼400 K. For $T >$ 400 K, the $(220)_{pc}$ profile looks like a doublet, as expected for the tetragonal phase, but the additional broadening of $(111)_{pc}$ rules this out. The temperature dependence of the FWHM of the $(111)_{pc}$ and $(200)_{pc}$ peaks is shown in Figs. 11 and 12 for PSZT530 and PSZT533, respectively. It is evident from these figures that for temperatures greater than 600 K, the FWHM of the $(200)_{pc}$ peak is nearly constant. Similarly, the FWHM of the $(111)_{pc}$ peak is constant for $T \gtrsim 550$ K. Both features imply that the tetragonal structure of PSZT530 and PSZT535 is stable in the temperature range 550 K $\lesssim T \lesssim$ 625 K. Below 550 K, the broadening of the $(111)_{pc}$ peak starts growing, suggesting the appearance of the monoclinic phase in the Cm space group as a coexisting phase. Lebail fits for PSZT530 have been shown in our previous paper,[6] which confirmed that the pseudotetragonal and pseudorhombohedral monoclinic phases coexist in PSZT530 from low temperatures up to $T \lesssim 550$ K and transform to the pure tetragonal phase at $T \simeq 550$ K. Thus, the sequence of phase transitions for PSZT530 and PSZT535 is pseudotetragonal monoclinic (Cm) + pseudorhombohedral monoclinic (Cm) to tetragonal ($P4mm$) and then tetragonal to cubic ($Pm\bar{3}m$).

Evolution of the $(111)_{pc}$, $(200)_{pc}$, and $(220)_{pc}$ profiles with temperature for PSZT with $x = 0.545$ (i.e., PSZT545) is shown in Fig. 13. The splitting of both $(111)_{pc}$ and $(200)_{pc}$ and anomalous broadening of $(200)_{pc}$ profiles are consistent with the pseudorhombohedral monoclinic phase in the Cm space group.[3] The splitting of the $(111)_{pc}$ and $(220)_{pc}$ peaks disappears ∼475 K, but the FWHM of the $(111)_{pc}$ and $(200)_{pc}$ peaks persists and decreases with increasing temperature, as shown in Figs. 14(a) and 14(b). The presence of additional broadening in the $(200)_{pc}$ peak and the disappearance of the broadening of the $(111)_{pc}$ peak in the temperature range 550 K $\leqslant T \leqslant$ 600 K suggests that $(200)_{pc}$ is still a doublet while $(111)_{pc}$ is a singlet

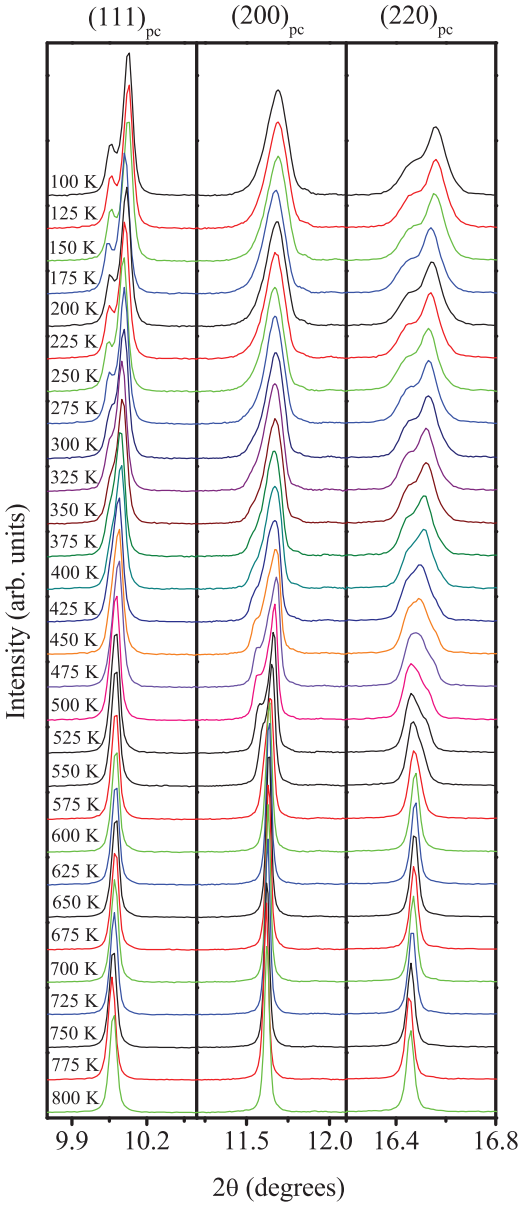

FIG. 10. (Color online) The evolution of synchrotron powder XRD profiles of the $(111)_{pc}$, $(200)_{pc}$, and $(220)_{pc}$ reflections of PSZT535 with temperature.

in this temperature range. Both imply a tetragonal structure in the temperature range 550 K $\lesssim T \lesssim$ 600 K. Above 600 K, the broadening of the $(200)_{pc}$ peak also disappears, implying the singlet nature of this and other peaks. This suggests that the structure is cubic for $T >$ 600 K. The broadening of the $(111)_{pc}$ peak below $T \simeq$ 550 K, eventually leading to splitting of the peak at lower temperatures, confirms that the pseudorhombohedral monoclinic (Cm) phase of PSZT545 transforms to the tetragonal ($P4mm$) phase at 525 K $\lesssim T \lesssim$ 550 K and that this tetragonal phase at still-higher temperatures ($T \gtrsim$ 600 K) transforms to the cubic ($Pm\bar{3}m$) phase.

Rietveld refinements for PSZT with $x = 0.550$ (PSZT550)[7] have confirmed the pure Cm phase structure at room temperature. It transforms to the Cc phase below room temperature through an AFD transition confirmed by neutron diffraction measurements.[7] The temperature dependence of $(111)_{pc}$,

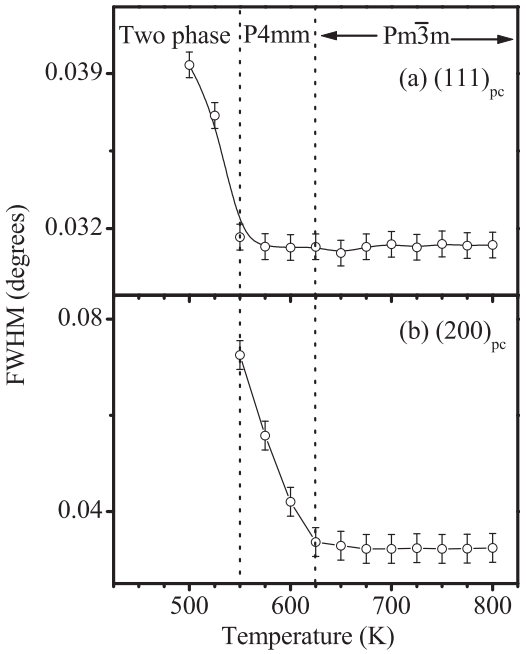

FIG. 11. The variation of FWHM of the (a) $(111)_{pc}$ and (b) $(200)_{pc}$ reflections of PSZT530 with temperature.

$(200)_{pc}$, and $(220)_{pc}$ peak profiles of PSZT550 is shown in Fig. 15. It is evident from this figure that the splitting of the peaks disappears above 450 K. However, the width of the peaks is still quite large and decreases with increasing temperature, as shown in Fig. 16 for the $(111)_{pc}$ and $(200)_{pc}$ peaks. This suggests that none of the peaks are singlets. However, at $T >$ 600 K, the FWHM of the both peaks is nearly temperature independent, suggesting that all peaks are now singlet as expected for the cubic phase. These results

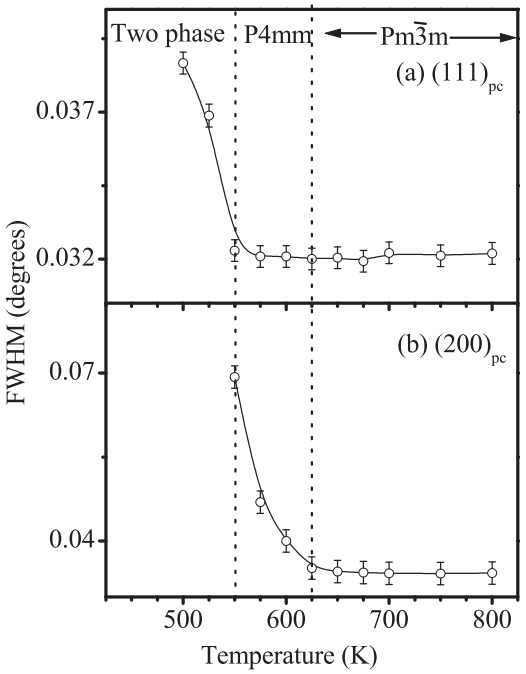

FIG. 12. The variation of FWHM of the (a) $(111)_{pc}$ and (b) $(200)_{pc}$ reflections of PSZT535 with temperature.

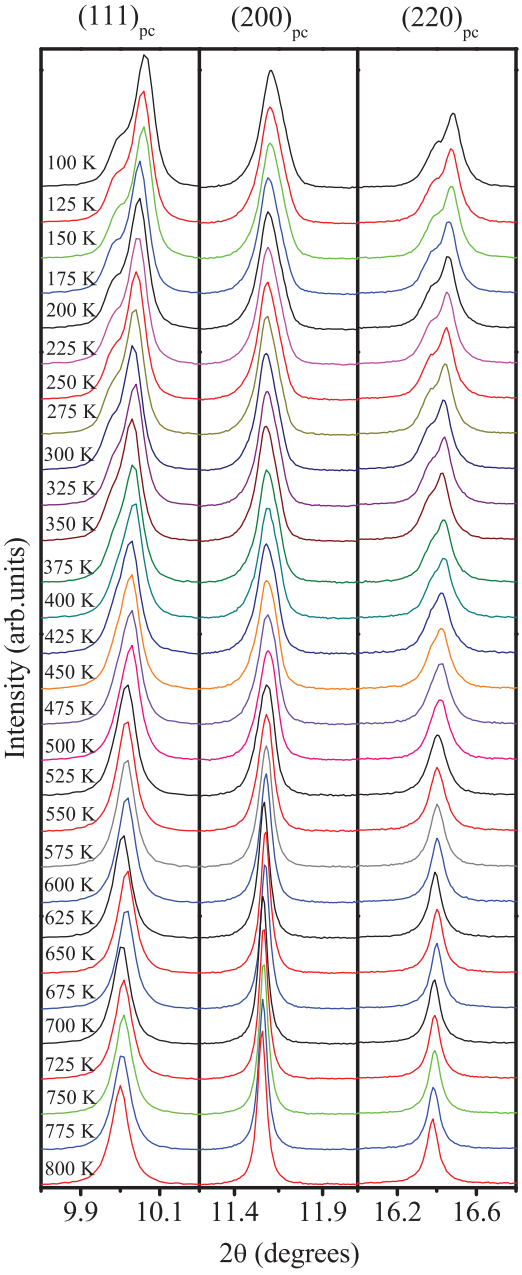

FIG. 13. (Color online) The evolution of synchrotron powder XRD profiles of the $(111)_{pc}$, $(200)_{pc}$, and $(220)_{pc}$ reflections of PSZT545 with temperature.

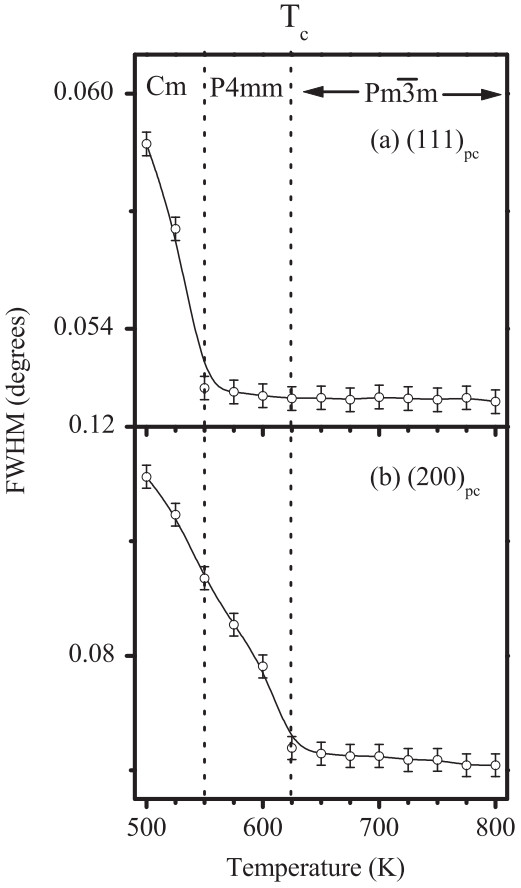

FIG. 14. The variation of FWHM of the (a) $(111)_{pc}$ and (b) $(200)_{pc}$ reflections of PSZT545 with temperature.

show that the pseudorhombohedral monoclinic (Cm) phase of PSZT550 transforms directly into the cubic phase.

All PSZT compositions discussed above undergo an AFD phase transition below room temperature, leading to the appearance of a superlattice peak in neutron powder diffraction patterns only. As a result of this AFD transition, the Cm space group structure changes to the Cc space group structure.[6,7] Since these superlattice peaks are not discernible in SXRD patterns below room temperature,[6,7] the SXRD data does not reveal the Cm-to-Cc AFD transition below room temperature. We have, therefore, in the discussions above, not distinguished between Cc and Cm space groups even at 100 K. Furthermore, the ferroelectric phase transition temperatures decrease slightly with increasing Zr^{4+} content in the composition range $0.515 \leqslant x \leqslant 0.550$ from ~614 K for $x = 0.515$ to 604 K for $x = 0.550$. However, since SXRD data were collected at 25 K intervals, several compositions appear to show transitions nearly at the same temperature as per the SXRD data.

From the above discussion, it is evident that the high-temperature cubic phase first transforms into a tetragonal phase for the PSZT composition with $x \leqslant 0.545$, whereas it transforms directly into a pseudorhombohedral monoclinic phase for $x = 0.550$. This suggests the existence of a triple point at $0.545 \lesssim x \lesssim 0.550$. The variation of unit cell parameters and unit cell volume over a limited temperature range, as obtained by Rietveld refinement of the structure at various temperatures, is shown in Fig. 17 for the cubic-to-tetragonal phase transition of PSZT with (a) $x = 0.515$, (b) $x = 0.520$, (c) $x = 0.525$, (d) $x = 0.530$, (e) $x = 0.535$, and (f) $x = 0.545$. It is evident from these figures that the cubic-to-tetragonal phase transition is accompanied with a discontinuous change in the unit cell volume at the transition temperature. This implies the first-order nature of the tetragonal-to-cubic phase transition, in agreement with the observation of thermal hysteresis in the dielectric measurements discussed earlier. The vertical lines at T_c are drawn to show the value of discontinuous change in the unit cell volume (ΔV) at T_c for the tetragonal-to-cubic phase transition determined by dielectric measurements during heating. Figure 2(b) shows the discontinuous change (ΔV) in the unit cell volume at the cubic-to-tetragonal phase transition temperature as a

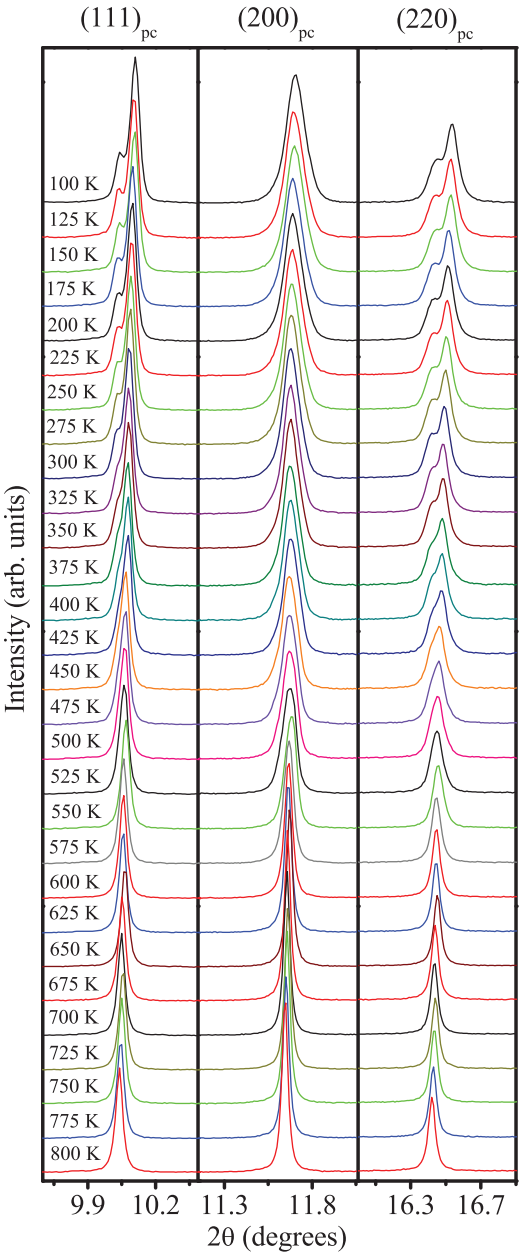

FIG. 15. (Color online) The evolution of synchrotron powder XRD profiles of the $(111)_{pc}$, $(200)_{pc}$, and $(220)_{pc}$ reflections of PSZT550 with temperature.

function of composition. It is evident from this figure that the extrapolated value of ΔV approaches zero for $x \simeq 0.550$. This is in agreement with the continuous variation of the unit cell volume across the cubic-to-monoclinic phase transition shown in Fig. 17(g) for $x = 0.550$. The vanishing of ΔV at $x \simeq 0.550$ coincides with the vanishing of the thermal hysteresis $\Delta T = ({T_c}^H - {T_c}^C)$ at $x \simeq 0.553$ in the dielectric studies [Fig. 2(a)]. Both clearly reveal a crossover from a first-order to a second-order phase transition with a tricritical point at $x \simeq 0.550$, which is also the triple point in the phase diagram of PSZT.

C. Landau-Devonshire theory considerations

We have determined the Landau-Devonshire free-energy curves as a function of composition with a view to visualize

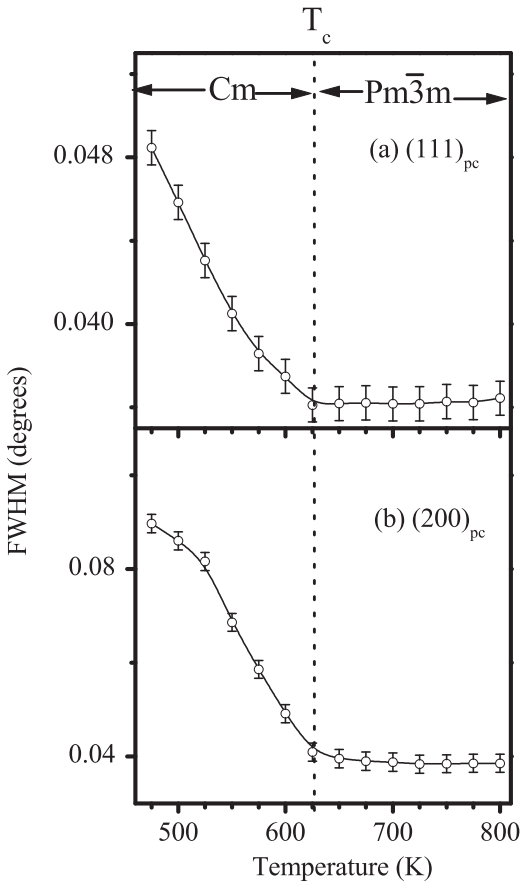

FIG. 16. The variation of FWHM of the (a) $(111)_{pc}$ and (b) $(200)_{pc}$ reflections of PSZT550 with temperature.

the flattening of the free-energy surface associated with the cubic-to-tetragonal phase transition on approaching the MPB from the tetragonal side. For this, we have considered the Landau-Devonshire free-energy function used by Haun *et al.*[22] to calculate the free energy of the tetragonal phase of PZT. For the free-energy tetragonal phase with polarization components $P_1 = P_2 = 0$, $P_3 \neq 0$, the free-energy function can be written as follows, under a zero stress condition:[22]

$$\Delta G = \alpha_1 P_3^2 + \alpha_{11} P_3^4 + \alpha_{111} P_3^6 \quad (1)$$

The coefficients α_{11} and α_{111} are assumed to be temperature independent; α_{11} is positive for the second-order phase transition and negative for the first-order phase transition, while α_{111} is always positive. The coefficient α_1 is assumed to have the following type of temperature dependence based on the Curie-Weiss law:

$$\alpha_1 = (T - T_0)/(2\varepsilon_0 C) = \alpha_0 (T - T_0) \quad (2)$$

where ε_0, C, and T_0 are the permittivity of free space, the Curie constant, and the Curie-Weiss temperature, respectively. Using the minimization condition $\partial G/\partial P_3 = 0$ and $\Delta G = 0$ at T_c, one obtains the following expressions for the remaining two coefficients:[22]

$$\alpha_{11} = -\frac{T_c - T_0}{\varepsilon_0 C P_{3c}^2} \quad (3)$$

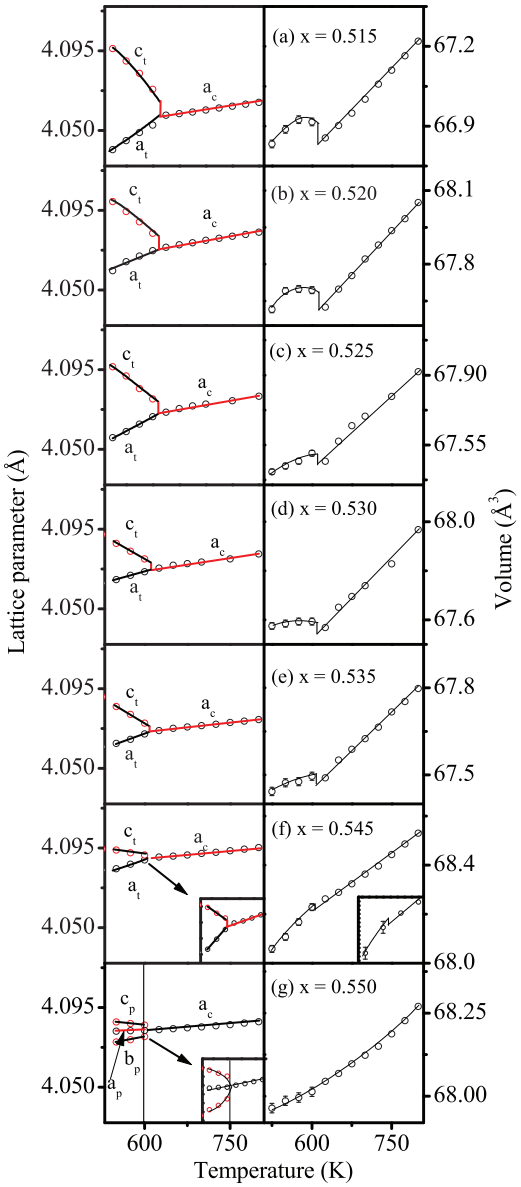

FIG. 17. (Color online) Variation of (a) a and c lattice parameters and (b) unit cell volume of various PSZT compositions with temperature. Error bars are less than the size of the data points. Continuous lines are visual guides.

and

$$\alpha_{111} = \frac{T_c - T_0}{2\varepsilon_0 C P_{3c}^4} \tag{4}$$

where P_{3c} is the value of spontaneous polarization at T_c. For a first-order phase transition, T_c is related to T_0 in the following manner:

$$T_c = T_0 + \alpha_{11}^2/(12\alpha_0\alpha_{111}) \tag{5}$$

The minimization condition $\partial G/\partial P_3 = 0$ yields the following expression for spontaneous polarization:

$$P_3^2 = [-\alpha_{11} + \sqrt{\alpha_{11} - 3\alpha_1\alpha_{111}}]/3\alpha_{111} \tag{6}$$

Substituting values of α_1, α_{11}, and α_{111} in above relation, we obtain the following expression for the spontaneous polarization:[22]

$$P_3^2 = \psi P_{3C}^2, \quad \text{where}$$

$$\psi = \left(\frac{2}{3}\right)\left\{1 + \left[1 - \frac{3(T - T_0)}{4(T_0 - T_c)}\right]^{\frac{1}{2}}\right\}. \tag{7}$$

The spontaneous transformation strains ($x_i = \partial G/\partial X_i$) under a zero stress condition were obtained using the procedure given by Haun *et al.*:[22]

$$x_1 = Q_{12} P_3^2 \tag{8}$$

$$x_3 = Q_{11} P_3^2 \tag{9}$$

Combining the above with Eq. (7), we get:

$$x_1 = x_{1c}\psi, \quad \text{where} \quad x_{1c} = Q_{12} P_{3c}^2 \tag{10}$$

$$x_3 = x_{3c}\psi, \quad \text{where} \quad x_{3c} = Q_{11} P_{3c}^2 \tag{11}$$

where x_{1c} and x_{3c} are the values of x_1 and x_3 at T_c, respectively.

Thus, ΔG as a function of temperature can be calculated from the knowledge of x_3, T_c, T_0, and C, all of which can be determined from the experimental data (see Haun *et al.*[22]) and Q_{11}. We now illustrate the determination of the coefficients in Eq. (1) using PSZT515 as an example. Lattice parameters corresponding to the cubic-to-tetragonal phase transition for PSZT515 are shown in Fig. 18(a). Lattice parameter a_c of the high-temperature cubic phase was extrapolated into the tetragonal region to obtain the extrapolated value a_c', which was used to calculate the spontaneous strain x_1 and x_3 for the tetragonal phase. The extrapolated values are shown with open circles in Fig. 18(a). The symmetry-adopted spontaneous

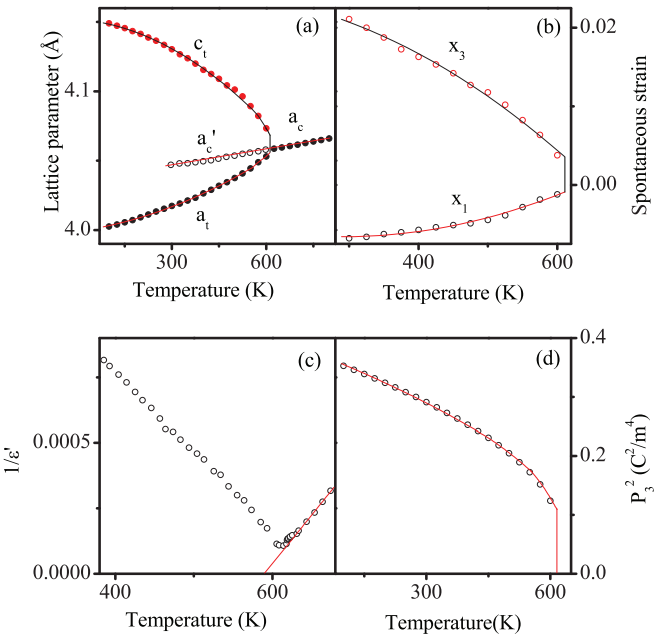

FIG. 18. (Color online) Temperature dependence of (a) the a and c lattice parameters (open dots represent the extrapolated values of a_c in the tetragonal region, and continuous lines are visual guides), (b) spontaneous strains x_1 and x_3 (continuous lines represent the least squares fit to the data points using a second-order polynomial), (c) dielectric stiffness ($\frac{1}{\varepsilon'}$) (the continuous line gives the Curie-Weiss fit), and (d) P_3^2 for PSZT515 (continuous lines are visual guides).

strains associated with the cubic-to-tetragonal phase transition are given by the following:

$$x_1 = \frac{a_t - a_c'}{a_c'} \quad \text{and} \tag{12}$$

$$x_3 = \frac{c_t - a_c'}{a_c'} \tag{13}$$

These were determined using the data given in Fig. 18(a) and are plotted in Fig. 18(b). From Eqs. (10) and (11), it is evident that the spontaneous strain is related to the temperature-dependent function ψ. The dependence of ψ on temperature is given by the following relationship [Eq. (7)]:[22]

$$\psi = \left(\frac{2}{3}\right)\left\{1 + \left[1 - \frac{3(T - T_0)}{4(T_0 - T_c)}\right]^{\frac{1}{2}}\right\},$$

ψ is thus a function of T_c and T_0, where T_c is the phase transition temperature and T_0 is the Curie-Weiss temperature. To calculate T_0, we have plotted $\frac{1}{\varepsilon'}$ vs T in Fig. 18(c), which also depicts the Curie-Weiss fit to the measured $\varepsilon'(T)$ data for PSZT515 above T_c. Since x_3 and ψ are related by $x_3 = x_{3c}\psi$, by fitting the spontaneous strain data (x_3) with ψ, we can calculate x_{3c}. Furthermore, $x_{3c} = Q_{11}P_{3c}^2$ and $P_3^2 = \psi P_{3c}^2$ [Eqs. (7) and (11)]. For Q_{11}, we have used the values given for PZT from Ref. 31 and calculated the spontaneous polarization P_{3c}^2. The obtained variation of P_{3c}^2, with temperature, is plotted in Fig. 18(d). For the compositions with $x = 0.520$ and 0.525, a similar procedure was adopted to calculate the various parameters. Figures 19 and 20 show the variation of lattice parameters, spontaneous strain, Curie-Weiss fit, and spontaneous polarization as a function of temperature

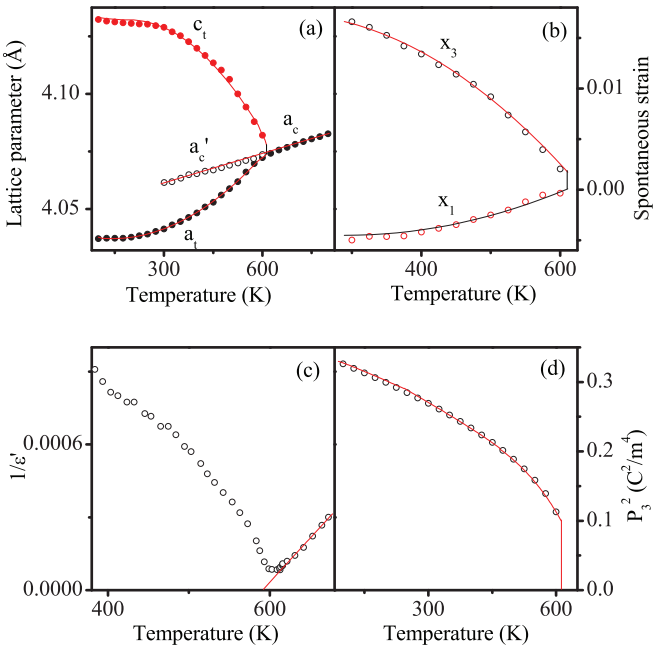

FIG. 19. (Color online) (a) Temperature dependence of (a) the a and c lattice parameters (open dots represent the extrapolated values of a_c in the tetragonal region, and continuous lines are visual guides), (b) spontaneous strains x_1 and x_3 (continuous lines represent the least squares fit to the data points using a second-order polynomial), (c) dielectric stiffness ($\frac{1}{\varepsilon'}$) (the continuous line gives the Curie-Weiss fit), and (d) P_3^2 for PSZT520 (continuous lines are visual guides).

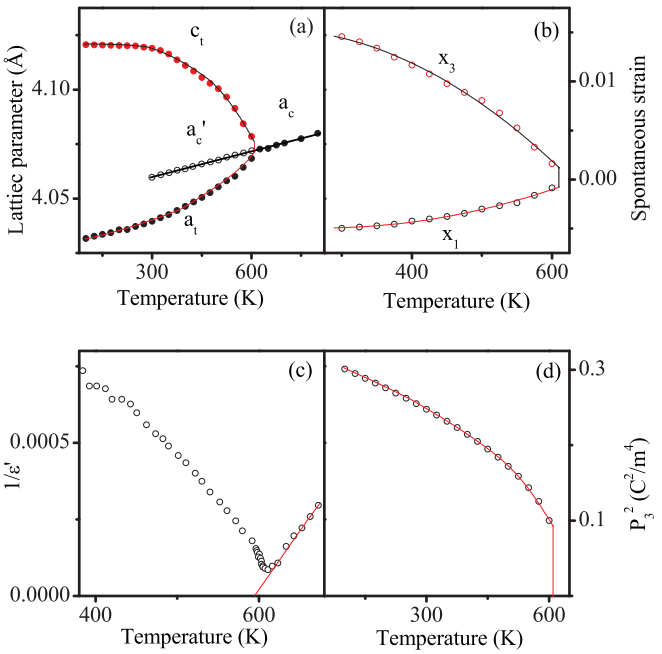

FIG. 20. (Color online) (a) Temperature dependence of (a) the a and c lattice parameters (open dots represent the extrapolated values of a_c in the tetragonal region, and continuous lines are visual guides), (b) spontaneous strains x_1 and x_3 (continuous lines represent the least squares fit to the data points using a second-order polynomial), (c) dielectric stiffness ($\frac{1}{\varepsilon'}$) (the continuous line gives the Curie-Weiss fit), and (d) P_3^2 for PSZT525 (continuous lines are visual guides).

corresponding to the tetragonal-to-cubic phase transition for PSZT520 and PSZT525, respectively.

We have calculated Landau coefficients using Eqs. (2)–(4). Various parameters used in Landau theory calculations are given in Table I. Using the Landau coefficients so determined, we calculated the free-energy density. Free-energy density as a function of polarization at several temperatures for PSZT515, PSZT520, and PSZT525 is plotted in Fig. 21. The energy barrier (ΔG_{Tc}) corresponding to the cubic-to-tetragonal thermodynamic phase transition temperature, at

TABLE I. Parameters obtained using the temperature dependence of cell parameters and dielectric constant.

Composition (x)	0.515	0.520	0.525
T_c (K)	614	612	611
T_0 (K)	589.353	590.1276	591.98
C (10^5 K)	2.681	2.7576	2.726
$T_c - T_0$	24.647	21.8724	19.02
x_{3c} (10^{-4})	91.06	87.00	78.04
Q_{11} (10^{-2} m^4/C^2)	9.468	9.355	9.224
P_{3c}^2 (10^{-2} C^2/m^4)	9.6176	9.30	8.46
α_{11} (10^8 m^5/C^{2}F)	−1.0801	−0.9636	−0.9319
α_{111} (10^8 m^9/C^{4}F)	5.6151	5.1811	5.5077
T_1 (K)	622.2157	619.2908	617.3400
T_2 (K)	648.5058	642.6214	637.6280
$(\Delta G)_{Tc}$[a] (10^6 J/m^3)	0.0740	0.0617	0.0494

[a]The energy barrier (ΔG) between the cubic and the tetragonal phases at the transition temperature (T_c).

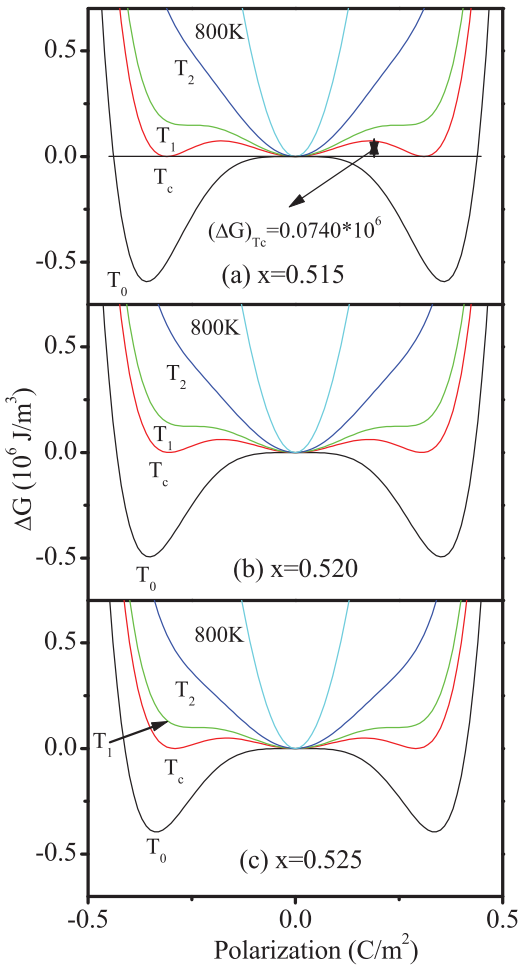

FIG. 21. (Color online) Gibbs free-energy profiles of PSZT515 calculated at different temperatures using Landau-Devonshire theory (Ref. 22). T_2 is the characteristic temperature at which the inflexion point in the free-energy profile develops, while for the temperature T_1, a local minimum for the tetragonal phase appears well above the thermodynamic phase transition temperature T_c, at which the free-energy profile is triply degenerate on account of coexistence of the tetragonal and cubic phases. At a temperature well below T_c, the minima corresponding to the tetragonal phase become global minima.

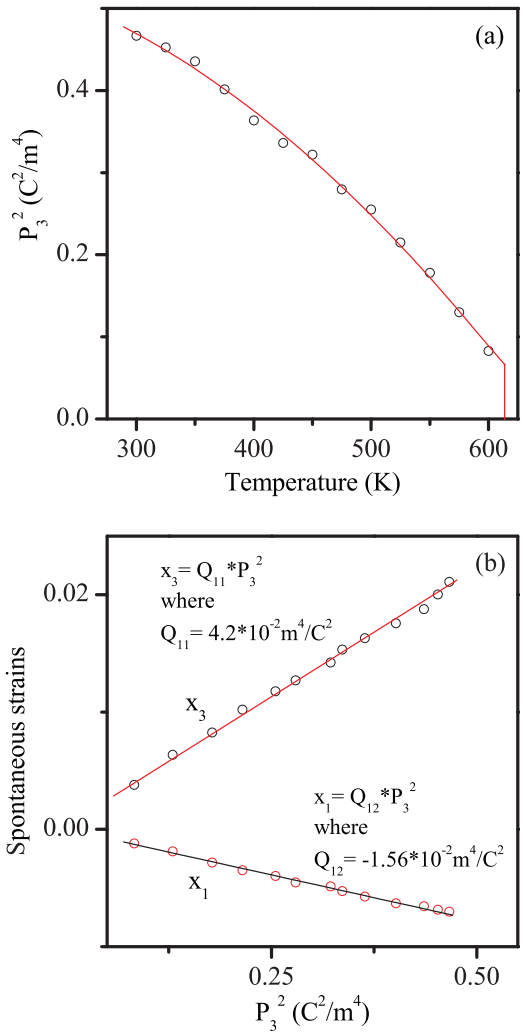

FIG. 22. (Color online) (a) Temperature dependence of P_3^2 and (b) variation of spontaneous strains (x_1, x_3) with P_3^2 for PSZT515. The continuous line gives the fit using the relation given in Eqs. (8) and (9). P_3^2 has been calculated from Born effective charges and atomic coordinates using Eq. (14).

which one observes triply degenerate minima in ΔG, were obtained from the free-energy plots. For a tricritical transition, this energy barrier $(\Delta G)_{Tc}$ should vanish, making the free-energy surface flat at the phase transition temperature. The variation of $(\Delta G)_{Tc}$ with composition is shown in Fig. 2(c). On extrapolating the linear behavior in Fig. 2(c), we find that the energy barrier $(\Delta G)_{Tc}$ vanishes for $x \simeq 0.550$. This reveals the flattening of the energy surface at T_c for $x \simeq 0.550$, as expected for a tricritical point predicted on the basis of dielectric and SXRD studies. Thus, Landau theory calculations confirm the findings, based on vanishing of thermal hysteresis in dielectric studies and the discontinuous change in unit cell volume in SXRD studies, that there exists a tricritical point at $x \simeq 0.550$, which is also the triple point in the PSZT phase diagram.

As is evident from Eqs. (8) and (9), Q_{11} and Q_{12} can also be obtained from the temperature dependence of spontaneous polarization (P_3) and spontaneous strain. We therefore calculated the spontaneous polarization using the atomic displacements ξ_i and Born effective charges Z_i for the cubic phase using the following relationship:

$$P = \frac{e}{V} \sum_i Z_i \xi_i \qquad (14)$$

where e is the charge of electron, V is the volume of the unit cell, and ξ_i the positional coordinates of the cations and anions obtained by Rietveld refinements. For the tetragonal phase of PSZT515 in the $P4mm$ space group, Pb/Sr atoms were kept fixed at the (0, 0, 0) position; they therefore do not contribute to the polarization. Values for Born effective charges for Zr, Ti, and oxygen were taken from Ref. 32. Polarization for PSZT515 has been calculated from the Rietveld refined coordinates and Born effective charges and has been plotted as a function of temperature in Fig. 22(a). In our calculations, for polarizations and spontaneous strains, we have used data from room temperature to high temperatures because of a phase transition to the monoclinic phase (see Sec. III D, phase diagram of PSZT, and Fig. 23) just below the room-temperature clear signature of

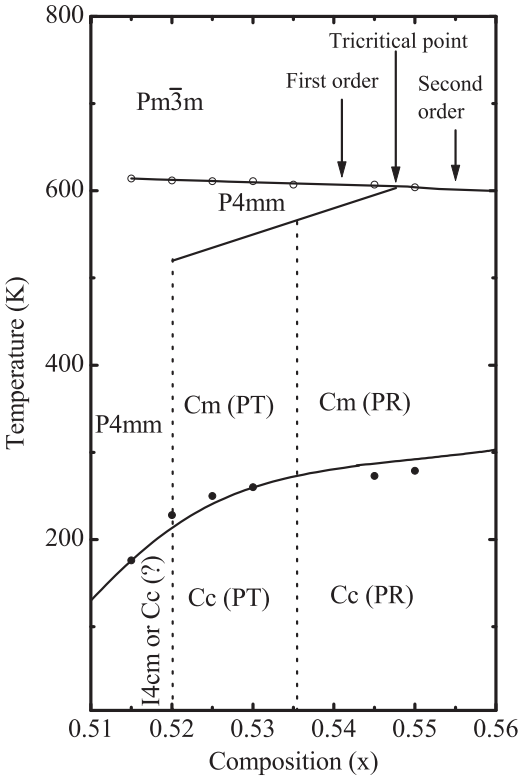

FIG. 23. Schematic phase diagram of PSZT around the MPB region constructed on the basis of present paper and earlier neutron and ultrasonic measurements (Refs. 6 and 7) on the same set of PSZT samples. Open circles in the phase diagram correspond to the high-temperature cubic ($Pm\bar{3}m$) to tetragonal ($P4mm$) phase transition temperature during heating, obtained from dielectric measurements. The filled circles correspond to low-temperature AFD phase (space group Cc) transition temperatures (Refs. 6 and 7). The symbols PT and PR represent pseudotetragonal and pseudorhombohedral monoclinic phases, respectively. The vertical lines are first-order phase boundaries across which the two neighboring phases coexist. Also, the inclined $P4mm$-Cm(PT)/Cm(PR) phase boundary is a first-order phase boundary. The phase boundary marked with a filled circle is linked with the AFD transition whose order (first or second) is unsettled.

two transitions below room temperature have been observed in the attenuation of sound velocity[33] but the diffraction pattern do not reveal such a transition. A similar situation exists in PZT515.[34] Variation of spontaneous strains (x_1 and x_3) for PSZT515 with temperature calculated from Eqs. (12) and (13) and temperature dependence of lattice parameters has been already shown in Fig. 18(b). Figure 22(b) depicts the variation of spontaneous strains (x_1 and x_3) with P_3^2. It shows linear dependence. We therefore use the relation $x_1 = Q_{12}P_3^2$ and $x_3 = Q_{11}P_3^2$ to fit the variation depicted in Fig. 22(b). Unlike thin films, where one has to consider higher-order electrostrictive coupling terms to fit the dependence of spontaneous strain on spontaneous polarization,[35] our results show a nice linear behavior in Fig. 22(b). Values of Q_{11} and Q_{12} so obtained using straight line fits are 4.2×10^{-2} and -1.56×10^{-2} m^4/C^2, respectively, which are less than those of pure PZT515 (Q_{11} for pure PZT $= 9.468 \times 10^{-2}$ m^4/C^2 and $Q_{12} = -4.468 \times 10^{-2}$ m^4/C^2) but are of the same order of magnitude. This difference in the Q_{11} and Q_{12} values may be due to 6% Sr doping in PZT or due to the inaccurate polarization values, since x rays are not ideally suited to accurately locating the lighter atoms like oxygen. We have calculated the values of P_{3c}^2 using Q_{11} and Q_{12}, which are found to be 21.68×10^{-2} and 21.67×10^{-2} C^2/m^4, respectively. As expected, both values of P_{3c}^2 are nearly equivalent. It is therefore evident that one can use Q_{11} or Q_{12} to calculate the free energy. We have chosen Q_{11} to calculate the free energy.

For the two-phase compositions, such as PSZT520 and PSZT525, which transform to the pure tetragonal phase for temperatures above 525 K, the stability region of the pure tetragonal phase is rather narrow (550 K $\leqslant T \leqslant$ 600 K). Since we collected SXRD data at 25 K intervals, we did not have sufficient data points to carry out the type of analysis presented in Fig. 22. Furthermore, the temperature variation of P_3^2 and x_3 over such a narrow temperature range close to T_c may not reflect the ideal functional form and may therefore introduce errors in the Q values. Since the change in Q with small variation in x from 0.515 to 0.520 and to 0.525 is rather small for PZT, we assume the Q value of PSZT515 for PSZT520 and PSZT525 and carried out the free-energy calculations. Fig. 2(d) depicts the variation of $(\Delta G)_{Tc}$ with x. It is evident from the figure that the dependence shown in Figs. 2(c) and 2(d) is qualitatively similar and reveals flattening of the energy surface with increasing x. The extrapolated x_c value at which $(\Delta G)_{Tc}$ vanishes comes out to be $x \simeq 0.546$ using the new set of values of electrostrictive coefficients, which is close to $x_c \simeq 0.550$ obtained using electrostrictive coefficients of pure PZT. Thus, our assumption to use Q_{11} values of pure PZT for PSZT is justifiable. We further compare the Landau coefficients of PSZT obtained using the two preceding approaches to that of pure PZT in Table II. The Landau coefficients are of the same order of magnitude as that of pure PZT using the two preceding approaches. Based on the results shown in Figs. 2(c) and 2(d), we may conclude that a tricritical point exists in PSZT for $0.545 < x \lesssim 0.550$ and that it coincides with the triple point in the PSZT phase diagram.

D. Phase diagram of PSZT around the MPB region

In pure PZT, MPB occurs at $x \approx 0.520$, for which the piezoelectric and dielectric responses are maximum,[1,3,18] whereas

TABLE II. Landau coefficients of PZT, PSZT obtained using Q_{11} values of PZT, and PSZT obtained using Q_{11} value of PSZT515.

Composition (x)	0.515	0.520	0.525
	PZT		
α_{11} (10^8 m^5/C^2F)	−0.546816	−0.582517	−0.623225
α_{111} (10^8 m^9/C^4F)	1.33568	1.43996	1.50386
	PSZT (calculated using Q_{11} of PZT)		
α_{11} (10^8 m^5/C^2F)	−1.0801	−0.9636	−0.9319
α_{111} (10^8 m^9/C^4F)	5.6151	5.1811	5.5077
	PSZT (calculated using Q_{11} of PSZT515)[a]		
α_{11} (10^8 m^5/C^2F)	−0.47912	−0.43267	−0.4243
α_{111} (10^8 m^9/C^4F)	1.1049	1.0444	1.1418

[a] Q_{11} was calculated using Eq. (9) and data given in Fig. 22.

it occurs at $x = 0.530$ for PSZT.[6] On the basis of the present high-resolution SXRD and dielectric studies, in conjunction with earlier neutron powder diffraction and sound velocity studies,[6,7] we have constructed a temperature (T) composition (x) phase diagram of PSZT around the MPB region shown in Fig. 23. It is evident from this figure that the ferroelectric-to-paraelectric phase transition temperature decreases with decreasing $PbZrO_3$ content, as expected for the lower transition temperature for $PbZrO_3$. The low-temperature phase boundary corresponds to the AFD phase transition and has been drawn using sound velocity measurements, which reveal anomalies at the phase transition temperature.[33] The AFD phase transition temperature increases upon increasing the Zr content. This shows the weakening of driving force for AFD transition with decreasing Zr^{4+} content upon approaching the MPB. For $x = 0.515$, using Rietveld refinement of SXRD data, we found that structure is tetragonal in the temperature range 100 K $\leqslant T \leqslant$ 614 K and that for $T > 614$ K, the structure is cubic. But sound velocity measurements confirm that this composition also undergoes a low-temperature phase transition ~180 K. In the absence of additional splitting of the $(220)_{pc}$ peak or splitting of the $(111)_{pc}$ peak below 180 K (Fig. 3), it is not possible to guess the structure of the low-temperature phase of PSZT515. A similar situation has been pointed out by Ragini *et al.*[34] for pure PZT with $x = 0.515$. The space group of the low-temperature phase of PSZT515 may be $I4cm$ (Ref. 36) or Cc^2, but more work is needed before making a choice. For $0.520 \lesssim x \lesssim 0.525$, tetragonal and pseudotetragonal phases in the $P4mm$ and Cm space groups coexist, while for $0.525 < x \lesssim 0.535$, pseudotetragonal and pseudorhombohedral monoclinic phases, both in the Cm space group, represent the phase coexistence region. For $x = 0.545$, the pseudorhombohedral monoclinic phase in the Cm space group is stable up to 525 K, above which it transforms to the tetragonal phase and finally to the cubic phase. For $x = 0.550$, the pseudorhombohedral monoclinic phase transforms directly to the cubic phase. The triple point where the paraelectric-to-ferroelectric boundary and MPB intersect occurs at $0.545 < x \lesssim 0.550$. The tricritical point in PSZT also occurs at $0.545 < x \lesssim 0.550$. The earlier paper by Mishra *et al.*[18] revealed a tricritical point at $x = 0.550$ for pure PZT as well. This shows that the MPB in PSZT is less tilted, i.e., more vertical, than pure PZT. Vertical MPB implies that temperature variation will always keep the material close to the MPB. Vertical MPB (Ref. 37) is ideally preferred over tilted, as the flat energy surface associated with the tricritical point may be nearly preserved even at room temperature. The more vertical nature of the MPB in PSZT may be the reason for the higher value of $d_{33} \approx 300$ pC/N in PSZT in comparison to pure PZT, for which it is ~180 pC/N.[38]

IV. CONCLUSIONS

We have investigated the nature of the ferroelectric phase transition using temperature-dependent dielectric and SXRD studies for compositions around the MPB of PSZT. Using dielectric studies, we have shown that Curie transition is of the first order for $x \leqslant 0.545$, whereas it has a second-order character for $x \gtrsim 0.550$. Using Rietveld analysis of temperature-dependent SXRD data, we have shown that the discontinuous change (ΔV) in the unit cell volume at the cubic-to-tetragonal phase transition decreases with increasing x and finally vanishes for $x \gtrsim 0.550$, revealing a crossover from the first-order character of the transition for $x \lesssim 0.545$ to the second order at $x \simeq 0.550$. The dielectric and SXRD results confirm the existence of a tricritical point for $0.545 < x \lesssim 0.550$, at which the first-order cubic-to-tetragonal line of phase transition, the second-order cubic-to-psuedorhombohedral monoclinic line of phase transition, and MPB intersect and give rise to a triple point. Free-energy barrier $(\Delta G)_{T_C}$ between the coexisting tetragonal and cubic phases at the thermodynamic phase transition temperature, calculated using Landau-Devonshire theory for the cubic-to-tetragonal phase transition of PSZT, decreases linearly and vanishes around $x \simeq 0.550$, as expected for a tricritical point. These calculations confirm the flattening of the free-energy surface around $x \simeq 0.550$. The flattening of the free-energy surface at high temperatures also leads to the flatter energy surface at room temperature[11] for MPB compositions and results in enhanced electromechanical[39] and piezoelectric response[38] in the vicinity of MPB for PSZT (Ref. 38), as expected on the basis of the polarization rotation mechanism.[8,11]

ACKNOWLEDGMENTS

D.P. and Y.K. acknowledge financial support from the Department of Science and Technology, government of India, and the Japan Society for the Promotion of Science, under the Indo-Japan Science Collaboration Program. The synchrotron radiation experiments were performed at the BL02B2 beamline of SPring-8 with the approval of the Japan Synchrotron Radiation Research Institute (Proposals No. 2011A1324 and No. 2011A0084). D.P. also acknowledges financial support from the J. C. Bose National Fellowship grant. We are thankful to the referee for his valuable comments and suggestions regarding the calculations of electrostrictive coefficients (Q_{11} and Q_{12}) which resulted in Fig. 22 and Table II.

[1]B. Jaffe, W. R. Cook, and H. Jaffe, *Piezoelectric Ceramics* (Academic Press, London, 1971), pp. 135.

[2]D. Pandey, A. K. Singh, and S. Baik, Acta Cryst. A **64**, 192 (2008).

[3]Ragini, R. Ranjan, S. K. Mishra, and D. Pandey, J. Appl. Phys. **92**, 3266 (2002); A. K. Singh, S. Yoon, S. Baik, N. Shin, and D. Pandey, Appl. Phys. Lett. **91**, 192904 (2007).

[4]D. Phelan, X. Long, Y. Xie, Z.-G. Ye, A. M. Glazer, H. Yokota, P. A. Thomas, and P. M. Gehring, Phys. Rev. Lett. **105**, 207601 (2010); S. Gorfman, D. S. Keeble, A. M. Glazer, X. Long, Y. Xie, Z.-G. Ye, S. Collins, and P. A. Thomas, Phys. Rev. B **84**, 020102(R) (2011); N. Zhang, H. Yokota, A. M. Glazer, and P. A. Thomas, Acta Cryst. B **67**, 386 (2011).

[5]J. Frantti, S. Ivanov, S. Eriksson, H. Rundlof, V. Lantto, J. Lappalainen, and M. Kakihana, Phys. Rev. B **66**, 064108 (2002); J. Frantti, J. Phys. Chem. B **112**, 6521 (2008).

[6]R. S. Solanki, A. K. Singh, S. K. Mishra, S. J. Kennedy. T. Suzuki, Y. Kuroiwa, C. Moriyoshi, and D. Pandey, Phys. Rev. B **84**, 144116 (2011); R. S. Solanki, S. K. Mishra, A. Senyshyn, S. Yoon,

S. Baik, N. Shin, and D. Pandey, Appl. Phys. Lett. **102**, 052903 (2013).
[7]R. S. Solanki, S. K. Mishra, A. Senyshyn, I. Ishii, C. Moriyoshi, T. Suzuki, Y. Kuroiwa, and D. Pandey, Phys. Rev. B **86**, 174117 (2012).
[8]H. Fu and R. E. Cohen, Nature **403**, 281 (2000).
[9]A. K. Singh, S. K. Mishra, Ragini, and D. Pandey, Appl. Phys. Lett. **92**, 022910 (2008).
[10]D. Vanderbilt and M. H. Cohen, Phys. Rev. B **63**, 094108 (2001).
[11]D. Damjanovic, J. Am. Ceram. Soc. **88**, 2663 (2005); IEEE Trans. Ultrason. Ferroelectr. Freq. Control **56**, 1574 (2009); Appl. Phys. Lett. **97**, 062906 (2010).
[12]M. Porta and T. Lookman, Phys. Rev. B **83**, 174108 (2011).
[13]B. Noheda, D. E. Cox, G. Shirane, J. A. Gonzalo, L. E. Cross, and S. E. Park, Appl. Phys. Lett. **74**, 2059 (1999); B. Noheda, J. A. Gonzalo, L. E. Cross, R. Guo, S.-E. Park, D. E. Cox, and G. Shirane, Phys. Rev. B **61**, 8687 (2000).
[14]A. K. Singh and D. Pandey, Phys. Rev. B **67**, 064102 (2003).
[15]A. K. Singh and D. Pandey, J. Phys. Condens. Matter **13**, L931 (2001); J. M. Kiat, Y. Uesu, B. Dkhil, M. Matsuda, C. Malibert, and G. Calvarin, Phys. Rev. B **65**, 064106 (2002).
[16]D. M. Hatch, H. T. Stokes, R. Ranjan, Ragini, S. K. Mishra, D. Pandey, and B. J. Kennedy, Phys. Rev. B **65**, 212101 (2002).
[17]W. Liu and X. Ren, Phys. Rev. Lett. **103**, 257602 (2009).
[18]S. K. Mishra, A. P. Singh, and D. Pandey, Philos. Mag. B **76**, 213 (1997); S. K. Mishra and D. Pandey, *ibid.* **76**, 227 (1997).
[19]T. H. Kim, J.-H. Ko, S. Kojima, A. A. Bokov, X. Long, and Z.-G. Ye, App. Phys. Lett. **100**, 082903 (2012).
[20]V. V. Eremkin, V. G. Smotrakov, and E. G. Fesenko, Ferroelectrics **110**, 137 (1990).
[21]B. Noheda, N. Cereceda, T. Iglesias, G. Lifante, J. A. Gonzalo, H. T. Chen, and Y. L. Wang, Phys. Rev. B **51**, 16388 (1995).
[22]M. J. Haun, E. Furman, S. J. Jang, and L. E. Cross, Ferroelectrics **99**, 13 (1989); M. J. Haun, E. Furman, H. A. Mckinstry, and L. E. Cross, *ibid.* **99**, 27 (1989); M. J. Haun, Z. Q. Zhuang, E. Furman, S. J. Jang, and L. E. Cross, *ibid.* **99**, 45 (1989).
[23]R. W. Whatmore, R. Clarke, and A. M. Glazer, J. Phys. C Solid State Phys. **11**, 3089 (1978).
[24]G. A. Rossetti Jr. and A. Navrotsky, J. Solid State Chem. **144**, 188 (1999).
[25]G. A. Rossetti Jr., A. G. Khachaturyan, G. Akcay, and Y. Ni, J. Appl. Phys. **103**, 114113 (2008).
[26]A. P. Singh, S. K. Mishra, D. Pandey, Ch. D. Prasad, and R. Lal, J. Mater. Sci. **28**, 5050 (1993).
[27]E. Nishibori, M. Takata, K. Kato, M. Sakata, Y. Kubota, S. Aoyagi, Y. Kuroiwa, M. Yamakata, and N. Ikeda, Nucl. Instrum. Meth. Phys. Res. A **467–468**, 1045 (2001).
[28]J. Rodriguez-Carvajal, Physica B **192**, 55 (1993).
[29]M. E. Lines and A. M. Glass, *Principle and Applications of Ferroelectrics and Related Materials* (Clarendon, Oxford, UK, 1977), pp. 78.
[30]B. Noheda and D. E. Cox, Phase Transit. **79**, 5 (2006).
[31]L. Q. Chen, in *Physics of Ferroelectrics: A Modern Perspective*, edited by K. M. Rabe, C. H. Ahn, and J.-M. Triscone, Vol. 105 (Springer-Verlag, Berlin, 2007), p. 363.
[32]L. Bellaiche and D. Vanderbilt, Phys. Rev. B **61**, 7877 (2000).
[33]R. S. Solanki, I. Ishii, T. Suzuki, and D. Pandey (unpublished).
[34]Ragini, S. K. Mishra, D. Pandey, H. Lemmens, and G. Van Tendeloo, Phys. Rev. B **64**, 054101 (2001); Ragini, Ph.D. Thesis, Thesis in Materials Science and Technology, Banaras Hindu University, Varanasi-221005, 2003.
[35]A. Kvasov and A. K. Tagantsev, Phys. Rev. B **87**, 184101 (2013).
[36]I. A. Kornev, L. Bellaiche, P.-E. Janolin, B. Dkhil, and E. Suard, Phys. Rev. Lett. **97**, 157601 (2006).
[37]J. Rödel, W. Jo, K. T. P. Seifert. E.-M. Anton, T. Granzow, and D. Damjanovic, J. Am. Ceram. Soc. **92**, 1153 (2009).
[38]R. Lal, R. Krishnan, and P. Ramakrishnan, Trans. Brit. Ceram. Soc. **87**, 99 (1988).
[39]S. K. Mishra, A. P. Singh, and D. Pandey, Appl. Phys. Lett. **69**, 1707 (1996).